

Multilayer nanoassembly of Sn-nanopillar arrays sandwiched between graphene layers for high-capacity lithium storage†

Liwen Ji,^a Zhongkui Tan,^a Tevye Kuykendall,^a Eun Ji An,^a Yanbao Fu,^b Vincent Battaglia^b and Yuegang Zhang^{*a}

Received 1st May 2011, Accepted 9th June 2011

DOI: 10.1039/c1ee01592c

Sn nanopillar arrays embedded between graphene sheets were assembled using a conventional film deposition and annealing process. The as-formed three-dimensional (3D) multilayered nanostructure was directly used as an anode material for rechargeable lithium-ion batteries without adding any polymer binder and carbon black. Electrochemical measurements showed very high reversible capacity and excellent cycling performance at a current density as high as 5 A g⁻¹. These results demonstrated that nanocomposite materials with highly functional 1D and 2D components can be synthesized by employing conventional top-down manufacturing methods and self-assembly principles.

Introduction

Elemental tin (Sn) is one of the most attractive alloying mechanism-based anode materials used for high performance rechargeable lithium-ion batteries (LIBs) because of its high theoretical specific capacity (992 mA h g⁻¹) and high operating voltage along with the absence of solvent intercalation.^{1–6} However, the huge volumetric expansion/shrinkage due to the alloying/dealloying reactions of Sn with lithium (Li) causes severe mechanical disintegration (such as cracking and pulverization), breakdown of the electrical conduction pathways in the electrodes, and even the loss of physical and electronic integrities of the active material. These enormous volume and structural changes lead to severe degradation of the electrodes upon cycling

and dramatically shorten the cycle life of the electrode. As a result, practically durable high-rate and high cycle life Sn-based electrodes have not yet been achieved.^{1–7} To address this problem, a variety of Sn and carbon nanocomposites with different geometrical attributes, morphological forms, and micro-structures have been explored,^{4,6,8–14} where the carbon matrices can play the role of buffering and accommodating the mechanical stress induced by the substantial volume expansion and shrinkage of the high-capacity Sn component. Therefore, the carbon matrices can, to a large extent, prevent deterioration, preserve the integrity, and thus avoid the failure of the electrodes upon consecutive Li-ion insertion/extraction cycles.^{4–6,8–14}

As a novel two-dimensional aromatic monolayer carbon, graphene has drawn special attention because of its outstanding and intriguing chemical, physical, and mechanical properties compared to other types of carbon materials.^{15–21} Graphene has recently been used to encapsulate several kinds of metal oxides and metals/semiconductors to fabricate novel nanocomposite electrodes for rechargeable LIBs and improved electrochemical behaviors were demonstrated.^{6,16–23} Despite this progress, further investigation on an optimized nanostructure in such

^aThe Molecular Foundry, Lawrence Berkeley National Laboratory, One Cyclotron Road, Berkeley, California, 94720, USA. E-mail: yzhang5@lbl.gov

^bAdvanced Energy Technology Department, Lawrence Berkeley National Laboratory, One Cyclotron Road, Berkeley, California, 94720, USA

† Electronic supplementary information (ESI) available. See DOI: 10.1039/c1ee01592c

Broader context

Rechargeable lithium-ion batteries (LIBs) are playing more and more important roles in our daily lives. However, their further improvements in the cycling time, safety, and energy/power densities are still highly required in order to meet the critical demand for powering more advanced hybrid electric vehicles (HEV) and plug-in hybrid electric vehicles (PHEV). For this point, the developments of novel nanostructured electrodes are urgently needed to replace the currently used bulk materials. In the current study, we utilized self-assembly and conventional film processing approaches to fabricate graphene/Sn-nanopillar multilayered nanostructures and also evaluate their electrochemical behaviors as binder-free anodes in rechargeable LIBs. Our explorations found that these fabricated novel nanostructures have high reversible Li storage capacity, improved cycling, and especially, excellent rate performance even at a very high current density.

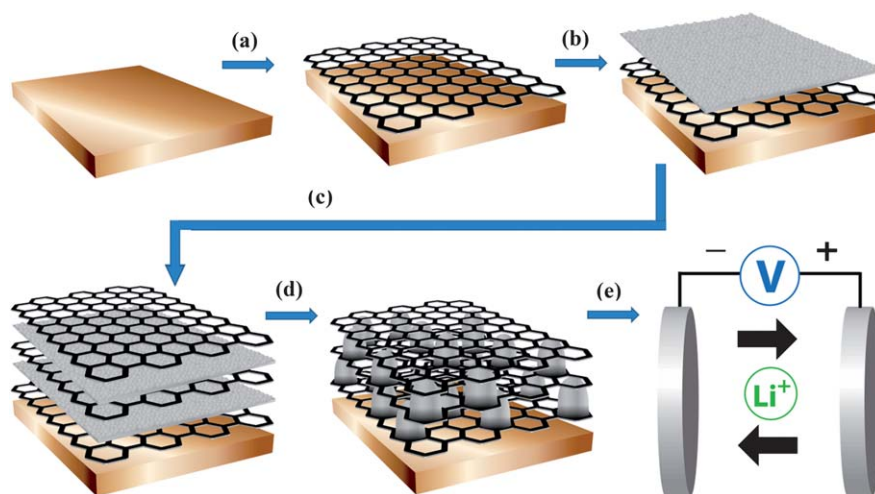


Fig. 1 Schematic illustration of the graphene/Sn-nanopillar nanostructure preparation procedures. (a) Transferring graphene film to a copper foil current collector; (b) depositing the Sn film on the transferred graphene surface *via* thermal evaporation; (c) repeating steps (a and b) followed by coating another layer of graphene; (d) thermal annealing of the as-formed nanostructure to obtain the multilayer graphene/Sn-nanopillar nanostructure; and (e) assembling Li-ion cells to evaluate the electrochemical performance of the graphene/Sn-nanopillar nanostructured electrodes.

nanocomposites is still much needed for achieving practically useful cycle life and rate capability for high performance LIB electrodes.

In this study, we assembled graphene/Sn-nanopillar multilayered nanocomposite anodes by employing both self-assembly and conventional film processing approaches (Fig. 1). In this rationally designed nanoarchitecture, the unique geometry of the self-assembled Sn nanopillar arrays with large Li-storage capacity can provide the most freedom for dimension changes and alleviate the mechanical stress/strain induced by the volume change during alloying/dealloying reactions.^{24,25} Similar to other reported well-ordered arrays of one-dimensional nanostructures,^{6,24–34} the unique Sn nanopillars can also enhance Li-ion insertion by reducing diffusion/migration barrier and allow easy penetration of the electrolyte between neighboring nanopillars and hence reduce internal resistance, which is particularly helpful for high energy/power applications. The addition of flexible and conductive graphene layers to the Sn nanopillar arrays can provide extra “cushion” for the structure to accommodate large volume change induced by Li–Sn alloying/dealloying reactions. Besides the mechanical merits, high electrical conductivity of both constituent materials and their distinctive structures in the nanocomposites can palliate the problems of the slow electrochemical kinetics and sluggish transport rate by offering high surface area and short diffusion pathway for more efficient transport of both electrons and Li-ions. In addition, graphene sheets also have considerable reversible Li-storage capacity because lithium could be stored not only on both sides of graphene, but also on their significant disorder, edges, vacancies, and covalent sites.^{15,16,18–20} As a result, these assembled graphene/Sn-nanopillar multilayered nanostructures may exhibit synergic properties and display superior electrochemical performance with large reversible capacity, excellent rate capability and cyclic performance, when used as anodes for rechargeable LIBs. Furthermore, polymer binders and conductive additives which are commonly used for other electrode materials are not needed

in such integrated electrodes, which will improve the overall energy density of the batteries.^{26,27,35}

Experimental

Chemicals

The graphite powder, *N*-methyl-2-pyrrolidone (NMP), sodium hydroxide (NaOH), and Sn powders were purchased from Sigma Aldrich. Anodic aluminium oxide (AAO) membrane was obtained from Whatman Inc.

Material preparations

In a typical experiment, graphite powders were exfoliated and dispersed in NMP solvent, at a concentration of 0.4 mg ml⁻¹ by sonicating in a power sonic bath (Model 75 D) for 120 minutes. The resulting dispersion was then centrifuged using an Allegra X-22 centrifuge for 30 minutes at 1000 rpm. After centrifugation, decantation was carried out by pipetting off the top half of the dispersion.³⁶ Afterwards, the prepared graphene NMP solution was filtrated directly using an AAO membrane with a pore size of 20 nanometres. The vacuum filtration of the as-prepared graphene dispersions in NMP resulted in the formation of a graphene film on the AAO membrane. After removing the AAO membrane with NaOH solution and rinsing with distilled water, the graphene film with a thickness of about 80–100 nm was directly transferred to a copper foil-based current collector. Afterwards, a Sn film was deposited on the as-prepared graphene film surfaces using a thermal evaporator in a high-purity nitrogen filled glove box. These processes were repeated to obtain two layers of Sn films embedded between three layers of graphene films. Finally, the as-fabricated graphene/Sn nanopillar multilayered nanostructures were annealed at 300 °C in Ar/H₂ (95/5) environments. For control samples, pure graphene films and pure Sn films were also prepared *via* the conventional film processing method and thermal evaporation, respectively, and

annealed at the same conditions. Here, in order to decrease the possible experimental error in the following electrochemical measurements, both the pure graphene and Sn films contained the same ingredients with the corresponding components in graphene/Sn multilayered nanostructures (so theoretically, both the mass of pure graphene films and Sn films should be the same with the corresponding components in the composite nanostructures).

Characterization

The samples were characterized by scanning electron microscopy (SEM: Zeiss Gemini Ultra-55) with energy dispersive X-ray spectroscopy (EDS), X-ray diffraction (Diffraktometer D500/501, Siemens) and Raman spectroscopy (Witec with a 532 nm green laser).

Electrochemical evaluation

2032 Coin-type half-cells were assembled using the prepared graphene/Sn-nanopillar nanostructures, pure graphene films, and thermal evaporated Sn films as the active materials in a high-purity argon-filled glove box. Thin Li foil (0.5 mm thick, FMC lithium) was employed as the counter electrode and a polypropylene membrane (Celgard 2400) was used as the separator. The electrolyte was 1 M lithium hexafluorophosphate (LiPF_6), dissolved in 1/1 (V/V) ethylene carbonate/ethyl methyl carbonate (EMC) (Ferro Corp.). Cyclic voltammogram (CV) measurements were performed on an AQ4 Gamry Reference 600 electrochemical workstation with a voltage range from 2 mV to 3.0 V at different scan rates of 0.05 or 0.1 mV s^{-1} . Galvanostatic charge and discharge experiments of the half-type coin cells were conducted using an Arbin automatic battery cycler at several different current rates between the cut-off potentials of 2 mV to 3.0 V.

Results and discussion

Fig. 1 schematically illustrates the fabrication process of the graphene/Sn-nanopillar multilayered nanocomposites (see Experimental section). Firstly, a graphene layer is transferred on a Cu foil following a filtration process using liquid phase exfoliated graphene dispersion in NMP solution. SEM image in Fig. S1† shows the top-view morphology of the graphene film, while Raman spectra in Fig. S2† indicate that the few-layer graphene flakes in the prepared film are quite different from the starting graphite powders. In addition, the relatively clean graphene films have an average thickness of about 80–100 nm (see Fig. S3–S5†, and the corresponding analysis). Thermal vapor deposition is then used to deposit a thin layer of Sn on the graphene layer, followed by transferring another layer of graphene to form a graphene/Sn/graphene sandwich structure. The last two coating steps can be repeated to form alternating graphene/Sn multilayers. A typical sample in this work consists of two alternating layers (if not specified otherwise), *i.e.*, two Sn layers embedded between three layers of graphene sheets. A critical final step of the fabrication process is a heat treatment at 300 °C in Ar and H_2 atmosphere. After this thermal treatment, we obtained a unique nanostructured graphene/Sn composite (Fig. 2, S6 and S7† show the existence of both graphene and Sn components after the annealing process). Comparing the SEM images of graphene/Sn

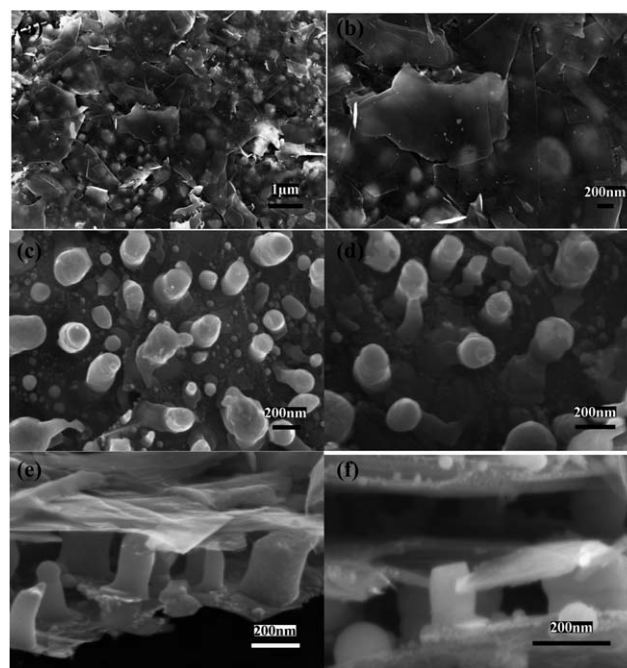


Fig. 2 SEM images of (a and b) top-views of the graphene/Sn-nanopillar nanostructures; (c and d) top-views of the Sn-nanopillars on graphene surfaces (after removal of the top graphene layers); (e and f) cross-sectional views of the graphene/Sn-nanopillar/graphene nanostructures.

nanopillar multilayered nanostructures before (Fig. S9†) and after (Fig. 2) the thermal treatment, we find that the Sn films with about 50 nm initial thickness undergo a morphological reorganization and self-assemble into Sn-nanopillar arrays sandwiched between graphene layers during the annealing process. The average thickness of the Sn layers (*i.e.* the height of nanopillar arrays) increases to about 150–200 nm after the annealing. The heights of Sn films and Sn-nanopillars are consistent with the distance between the sandwiching graphene layers, both before and after heat treatment, indicating that the distance between the top and bottom graphene layers changes to accommodate the height change of the Sn layer. We believe this effect also occurs during electrochemical cycling when graphene layers can accommodate the volume change in Sn and therefore improve the electrochemical performance of the electrode.

The formation of Sn-nanopillar from Sn films is very unique. Although the detailed formation mechanism is complex and need further investigation, we think the key factors are wettability and surface energy minimization during both Sn deposition and the post-annealing process. The poor wettability of Sn on the graphene surface results in Sn-nanoparticle-like structure formation during the thermal evaporation,^{37,38} as clearly observed in Fig. S9† (in contrast with the much larger Sn domains on the Cu surface, as shown in Fig. S8†). During the annealing process with a temperature above the melting point of Sn, the nanoparticulated Sn merges and forms nanopillars in order to reduce their surface energy. The formation of higher-aspect-ratio cylindrical nanopillars instead of spherical nanoparticles is due to the additional interface formation with the top graphene layers in the multilayered stacking structure (in contrast with the low-aspect-ratio nanoparticles formed during evaporation when

there is only one interface formation between Sn and the bottom graphene layers).

SEM images in Fig. 2(a) and (b) show the top-views of the annealed nanocomposites. The top graphene layer consists of randomly stacked micron-sized graphene sheets under which Sn nanopillars are visible. Fig. 2(c) and (d) are the top-views of Sn nanopillars, where the top graphene layer is removed. Most of the nanopillars have a diameter between 150 nm and 200 nm. The cross-sectional SEM images in Fig. 2(e) and (f) clearly show the Sn nanopillars sandwiched between two graphene layers. Most of the Sn nanopillars shown have both ends directly connected to the graphene. This is in contrast with the graphene/Sn multilayered structure before the thermal annealing process, where the Sn film has a low-aspect-ratio grainy structure typical for low-melting-point metal films deposited on non-wetting surfaces (see Fig. S9 in the ESI†). The intimate contact between Sn nanopillars and graphene layers enables a robust three-dimensional (3D) electron conduction network which is also mechanically flexible enough to buffer the huge volume change in the electrodes during continuous charge/discharge processes.

The obtained graphene/Sn multilayered nanocomposites, containing about 70 wt% Sn and 30 wt% graphene, were directly

used as binder-free anodes for rechargeable LIBs. Fig. 3(a) shows the CV of a half-cell using the multilayered graphene/Sn-nanopillar nanocomposite electrode. The broad cathodic peaks at 0.3–0.7 V can be attributed to multistep electrochemical reduction reactions (lithiation) of Sn with Li to form various Li–Sn alloys (Li_xSn_y). The difference near 0.7 and 1 V between the first and the following scans indicates a different initial lithiation route for the first cycle. The cathodic peak at 1 V in the first scan may be due to the formation of the solid electrolyte interphase (SEI) films or the irreversible reduction in the tin oxide (SnO_2) impurities.³⁹ The anodic scanning curves exhibit four distinct peaks at 0.4–0.8 V, which originate from the delithiation of the formed Li_xSn_y alloy phases.^{4,11,39–41} The discernible reduction and oxidation peaks at 0.1–0.2 V, which are observed for the graphene/Sn-nanopillar nanocomposite electrode but are absent for the pure Sn control samples (Fig. S10†), are attributed to the insertion/extraction of Li into/from graphene.^{18,20}

Fig. 3(b) shows the galvanostatic charge/discharge cycling result performed at a current density of 0.05 A g^{-1} with cutoff potentials at 2 mV and 3 V. The first charge profile presents a steep voltage drop to about 1 V and a long voltage plateau at about 1 V *versus* Li^+/Li , which is repeatable in other similar cells (Fig. S11†), indicating that at least some of the metallic Sn nanopillars are exposed to the electrolyte (not encapsulated inside the graphene layers), it may also be ascribed to the existed SnO_2 impurity.^{4,42,43} The plateau is followed by a sloping curve down to the cutoff voltage of 2 mV, delivering a large specific capacity of about 945 mA h g^{-1} . The first discharge profile reveals several voltage plateaus that are associated with different stages of phase transition from Li_xSn_y to Sn.^{8,18,42–45} The initial discharge capacity was found to be 734 mA h g^{-1} . The relatively small irreversible capacity of about 211 mA h g^{-1} could be attributed to the formation of the SEI layer on the electrode surface, because the decomposition of electrolyte always be involved in the electrode and electrolyte interface in the initial several cycles to form a covering passivation film on the electrode surface, this formation processes will consume Li-ions and lead to a decreased reversible capacity.^{8,42,44,46–48} At the second charge/discharge cycle, the multilayer anode still has a large reversible capacity of about 714 mA h g^{-1} , which indicates a high capacity retention rate of 97.3% from the first cycle. After 15th and 30th cycles, the reversible capacities are preserved at about 723 and 679 mA h g^{-1} (98.4 and 92.5% retention rates from the first cycle), respectively, indicating very slow capacity decay. This result is superior to the prior reported results of Sn/carbon nanocomposites.^{4,10,13,39,43} We attribute the significantly enhanced performance of the unique graphene/Sn-nanopillar multilayered nanostructure that enables reliable electrical contact and mechanical buffer to local volume changes, and thus maintain the integrities of the electrodes during cycling. This conclusion is further supported by the results obtained from control anode samples made by pure Sn films and pure graphene papers. Fig. 3(c) shows a comparison of the cycling performance of these single-component anodes with our multilayered graphene/Sn-nanopillar nanocomposite anodes. Even though the first discharge capacity of the pure Sn electrode is about 756 mA h g^{-1} which is comparable with the value of graphene/Sn-nanopillar nanocomposite, further cycling leads to a rapid capacity decay to 158 mA h g^{-1} after 30 cycles. Huge volume expansion/shrinkage

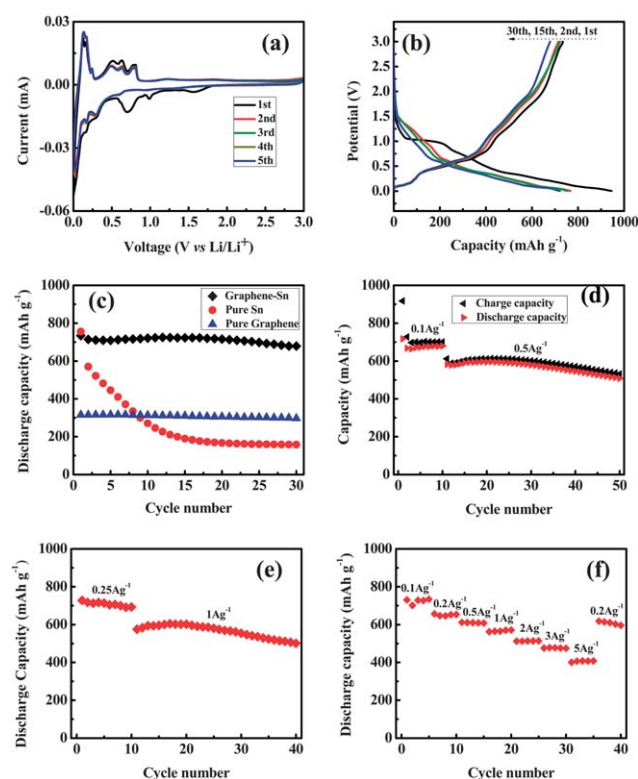


Fig. 3 (a) CV curve of a multilayered graphene/Sn-nanopillar nanostructure anode at 0.05 mV s^{-1} scanning rate. Galvanostatic charge/discharge profiles (b) and cycling performance (c) of graphene/Sn-nanopillar nanostructure anodes at a constant current density of 0.05 A g^{-1} . For comparison, the cycling performance of pure graphene and Sn films under the same conditions was also shown in (c). Cycling stabilities of the graphene/Sn-nanopillar nanostructures at high currents of 0.5 A g^{-1} (d), and 1 A g^{-1} (e), respectively; (f) reversible capacity *vs.* current density (rate capability) for graphene/Sn-nanopillar nanostructures. All the half-cells were cycled in the potential window from 2 mV to 3.0 V.

during the continuous alloying/dealloying reactions and the absence of graphene buffer layers may damage the structural integrity of pure Sn-based anodes, lead to the loss of electrical contact, and result in rapid capacity fading. The pure graphene paper shows a stable cycling performance, but with a relatively low first cycle discharge capacity of about 314 mA h g⁻¹, which decreases to 296 mA h g⁻¹ at 30th cycle (*i.e.*, 94.3% retention of the initial capacity). The comparison result shows that our multilayered graphene/Sn-nanopillar nanocomposite anodes can combine the merits of both graphene and Sn components and display both large Li-storage capability and excellent cycle performance.

Further cycling tests show that the graphene/Sn-nanopillar nanocomposite electrodes also exhibit excellent cycle life and rate capability at higher current densities. As shown in Fig. 3(d), the capacity remains constant at around 680 mA h g⁻¹ after the first ten cycles at a constant current of 0.1 A g⁻¹. Although the capacity decreases to about 582 mA h g⁻¹ upon subsequent cycling at a higher current of 0.5 A g⁻¹, the capacity remains stable at about 508 mA h g⁻¹ after 40 cycles. Fig. 3(e) shows cycling of another multilayer anode at a high current of 1 A g⁻¹ after the initial ten cycles at 0.25 A g⁻¹ current density. The capacity at 1 A g⁻¹ current is about 576 mA h g⁻¹ in the first cycle and 501 mA h g⁻¹ after 30 cycles, indicating a relatively slow capacity fading. Another example of the remarkable high-rate capability of our multilayer electrode is demonstrated in Fig. 3(f) where a half-cell retains a capacity of 408 mA h g⁻¹ at a current density as high as 5 A g⁻¹ after 35 cycles of variable current rates. This value is higher than the theoretical capacity of commercially used graphite anodes (*e.g.* 372 mA h g⁻¹).^{13,18,19,41,49} Further charge/discharge process at a current density of 0.2 A g⁻¹ brings it back to a high reversible capacity of 618 mA h g⁻¹. To our knowledge, there are still few reports that evaluate the electrochemical behaviors of Sn/C nanocomposite-based electrodes at such high current densities.¹² These results further demonstrate that the rationally designed graphene/Sn-nanopillar nanostructures can combine the excellent electronic conductivity of graphene and the high electrochemical capacity of Sn to achieve better performance in rechargeable LIBs.

As mentioned before, one of the main reasons for the poor cyclic life and disappointing rate capability of Sn-based electrodes is due to the huge volume change induced by the alloying/dealloying reactions of Li and Sn, which leads to the pulverization and the subsequent electrical and structural disconnections.^{5,9,11,18,42,46} The uniquely assembled graphene/Sn-nanopillar nanostructures of 1D Sn nanopillars and 2D graphene layers can enable efficient transport of both Li-ions and electrons while offering the most morphological flexibility to hamper the structural failure during cycling. The flexible and electrically conductive porous graphene layers in our unique hierarchical architecture electrodes can effectively bridge the active Sn components both electrically and mechanically. Meanwhile, the Sn nanopillars between different graphene layers (which are also electrochemically active) can work as spacers to reduce the restacking of different graphene layers. The large void volume in the structure not only allows easy penetration of the electrolyte resulting in a short Li-ion pathway, but also helps to accommodate the large volume change during Li insertion/extraction resulting in better cycle capability. The 3D porous conductive

channels in the structure reduce the inner resistance of the cells and are favorable for the improvement of the Li-ion electrochemical kinetics and hence the rate capability.^{17,19–21,24,50,51}

In conclusion, we fabricated a multilayered graphene/Sn-nanopillar nanostructure by employing both self-assembly and conventional film processing approaches, and tested its electrochemical performance as anode materials for rechargeable LIBs. In this rationally designed binder-free anode, both Sn and graphene serve as active Li storage materials, electronic conductive materials, as well as mechanically supporting materials. The unique structure buffers the huge volume change and preserves the electrode integrity upon continuous charge/discharge cycles, while enabling efficient ion and electron transport at the same time. As a result, the assembled bi-component nanostructure exhibits improved electrochemical performance, such as high specific capacity, better cycling life, and high rate capability up to 5 A g⁻¹.

Acknowledgements

This work was supported by the Office of Science, Office of Basic Energy Sciences, of the U. S. Department of Energy under contract No. DE-AC02-05CH11231.

Notes and references

- C.-M. Park, J.-H. Kim, H. Kim and H.-J. Sohn, *Chem. Soc. Rev.*, 2010, **39**, 3115–3141.
- W.-J. Zhang, *J. Power Sources*, 2011, **196**, 877–885.
- M. G. Kim and J. Cho, *Adv. Funct. Mater.*, 2009, **19**, 1497–1514.
- D. Deng and J. Y. Lee, *Angew. Chem., Int. Ed.*, 2009, **48**, 1660–1663.
- K. T. Lee, Y. S. Jung and S. M. Oh, *J. Am. Chem. Soc.*, 2003, **125**, 5652–5653.
- L. Ji, Z. Lin, M. Alcoutlabi and X. Zhang, *Energy Environ. Sci.*, 2011, DOI: 10.1039/c1030ee00699h, in press.
- D. Deng, M. G. Kim, J. Y. Lee and J. Cho, *Energy Environ. Sci.*, 2009, **2**, 818–837.
- Y. Qiu, K. Yan and S. Yang, *Chem. Commun.*, 2010, **46**, 8359–8361.
- M. Noh, Y. Kwon, H. Lee, J. Cho, Y. Kim and M. G. Kim, *Chem. Mater.*, 2005, **17**, 1926–1929.
- G. Derrien, J. Hassoun, S. Panero and B. Scrosati, *Adv. Mater.*, 2007, **19**, 2336–2340.
- W.-M. Zhang, J.-S. Hu, Y.-G. Guo, S.-F. Zheng, L.-S. Zhong, W.-G. Song and L.-J. Wan, *Adv. Mater.*, 2008, **20**, 1160–1165.
- Y. Yu, L. Gu, C. Wang, A. Dhanabalan, P. A. van Aken and J. Maier, *Angew. Chem., Int. Ed.*, 2009, **48**, 6485–6489.
- G. Cui, Y.-S. Hu, L. Zhi, D. Wu, I. Lieberwirth, J. Maier and K. Müllen, *Small*, 2007, **3**, 2066–2069.
- H. Li, Q. Wang, L. Shi, L. Chen and X. Huang, *Chem. Mater.*, 2002, **33**, 103–108.
- M. Liang and L. Zhi, *J. Mater. Chem.*, 2009, **19**, 5871–5878.
- H. Wang, L.-F. Cui, Y. Yang, H. Sanchez Casalongue, J. T. Robinson, Y. Liang, Y. Cui and H. Dai, *J. Am. Chem. Soc.*, 2010, **132**, 13978–13980.
- S. Yang, X. Feng, S. Ivanovici and K. Müllen, *Angew. Chem., Int. Ed.*, 2010, **49**, 8408–8411.
- G. Wang, B. Wang, X. Wang, J. Park, S. Dou, H. Ahn and K. Kim, *J. Mater. Chem.*, 2009, **19**, 8378–8384.
- J. Zhu, T. Zhu, X. Zhou, Y. Zhang, X. W. Lou, X. Chen, H. Zhang, H. H. Hng and Q. Yan, *Nanoscale*, 2011, **3**, 1084–1089.
- Z.-S. Wu, W. Ren, L. Wen, L. Gao, J. Zhao, Z. Chen, G. Zhou, F. Li and H.-M. Cheng, *ACS Nano*, 2010, **4**, 3187–3194.
- Y. Sun, Q. Wu and G. Shi, *Energy Environ. Sci.*, 2011, **4**, 1113–1132.
- L. Ji, Z. Tan, T. R. Kuykendall, S. Aloni, S. Xun, E. Lin, V. Battaglia and Y. Zhang, *Phys. Chem. Chem. Phys.*, 2011, **13**, 7170–7177.
- M. Pumera, *Energy Environ. Sci.*, 2011, **4**, 668–674.
- R. Liu, J. Duay and S. B. Lee, *Chem. Commun.*, 2011, **47**, 1384–1404.
- Y. Li, B. Tan and Y. Wu, *Nano Lett.*, 2007, **8**, 265–270.

- 26 L. Bazin, S. Mitra, P. L. Taberna, P. Poizot, M. Gressier, M. J. Menu, A. Barnabé, P. Simon and J. M. Tarascon, *J. Power Sources*, 2009, **188**, 578–582.
- 27 P. L. Taberna, S. Mitra, P. Poizot, P. Simon and J. M. Tarascon, *Nat. Mater.*, 2006, **5**, 567–573.
- 28 C. K. Chan, H. Peng, G. Liu, K. McIlwrath, X. F. Zhang, R. A. Huggins and Y. Cui, *Nat. Nanotechnol.*, 2008, **3**, 31–35.
- 29 Y.-S. Hu, X. Liu, J.-O. Müller, R. Schlögl, J. Maier and D. S. Su, *Angew. Chem., Int. Ed.*, 2009, **48**, 210–214.
- 30 Y. Wang and G. Cao, *Adv. Mater.*, 2008, **20**, 2251–2269.
- 31 D. Liu and G. Cao, *Energy Environ. Sci.*, 2010, **3**, 1218–1237.
- 32 F.-F. Cao, Y.-G. Guo and L.-J. Wan, *Energy Environ. Sci.*, 2011, **4**, 1634–1642.
- 33 L. Ji, Z. Lin, A. J. Medford and X. Zhang, *Chem.–Eur. J.*, 2009, **15**, 10718–10722.
- 34 L. Ji and X. Zhang, *Energy Environ. Sci.*, 2010, **3**, 124–129.
- 35 Z. Wang, F. Su, S. Madhavi and X. W. Lou, *Nanoscale*, 2011, **3**, 1618–1623.
- 36 Y. Hernandez, V. Nicolosi, M. Lotya, F. M. Blighe, Z. Sun, S. De, I. T. McGovern, B. Holland, M. Byrne, Y. K. Gun'ko, J. J. Boland, P. Niraj, G. Duesberg, S. Krishnamurthy, R. Goodhue, J. Hutchison, V. Scardaci, A. C. Ferrari and J. N. Coleman, *Nat. Nanotechnol.*, 2008, **3**, 563–568.
- 37 Y. Zhang, N. W. Franklin, R. J. Chen and H. Dai, *Chem. Phys. Lett.*, 2000, **331**, 35–41.
- 38 Y. Zhang and H. Dai, *Appl. Phys. Lett.*, 2000, **77**, 3015–3017.
- 39 M. Marcinek, L. J. Hardwick, T. J. Richardson, X. Song and R. Kostecki, *J. Power Sources*, 2007, **173**, 965–971.
- 40 M. Winter and J. O. Besenhard, *Electrochim. Acta*, 1999, **45**, 31–50.
- 41 L. Ji, Z. Lin, B. Guo, A. J. Medford and X. Zhang, *Chem.–Eur. J.*, 2010, **16**, 11543–11548.
- 42 D. Deng and J. Y. Lee, *J. Mater. Chem.*, 2010, **20**, 8045–8049.
- 43 Y. S. Jung, K. T. Lee, J. H. Ryu, D. Im and S. M. Oh, *J. Electrochem. Soc.*, 2005, **152**, A1452–A1457.
- 44 X. W. Lou, C. M. Li and L. A. Archer, *Adv. Mater.*, 2009, **21**, 2536–2539.
- 45 J. C. Lytle, H. Yan, N. S. Ergang, W. H. Smyrl and A. Stein, *J. Mater. Chem.*, 2004, **14**, 1616–1622.
- 46 H.-X. Zhang, C. Feng, Y.-C. Zhai, K.-L. Jiang, Q.-Q. Li and S.-S. Fan, *Adv. Mater.*, 2009, **21**, 2299–2304.
- 47 S. Zhang, M. S. Ding, K. Xu, J. Allen and T. R. Jow, *Electrochem. Solid-State Lett.*, 2001, **4**, A206–A208.
- 48 H. Buqa, A. Würsig, J. Vetter, M. E. Spahr, F. Krumeich and P. Novák, *J. Power Sources*, 2006, **153**, 385–390.
- 49 L. Ji, K.-H. Jung, A. J. Medford and X. Zhang, *J. Mater. Chem.*, 2009, **19**, 4992–4997.
- 50 N. A. Kaskhedikar and J. Maier, *Adv. Mater.*, 2009, **21**, 2664–2680.
- 51 K. Saravanan, K. Ananthanarayanan and P. Balaya, *Energy Environ. Sci.*, 2010, **3**, 939–948.